Ultra-Low Power System for Atrioventricular Synchronization Using Leadless Pacemakers

Mirko Maldari[1], Chadi Jabbour[1], Youcef Haddab[2], and Patricia Desgreys[1]

[1]LTCI, Télécom Paris
Institut Polytechnique de Paris
19 place Marguerite Perey, 91120 Palaiseau France
E-mail: mirko.maldari@gmail.com

[2]Microport CRM
4 Avenue Réaumur, 92140 Clamart, France

Abstract

Leadless cardiac pacemakers (LCP) are the cutting-edge technology of cardiac rhythm management (CRM), reducing complication risks and treatment invasivity. Current leadless cardiac pacemakers can only pace a single location of the heart, limiting their use to a small fraction of the bradycardia patient population. A dual-chamber system of synchronized leadless cardiac pacemakers is required to cover the major part of bradycardia patients. The power consumption relating the synchronization of pacemaker nodes is one of the major technological challenges preventing the rise of dual-chamber leadless cardiac pacemaker systems. Intra-body communication (IBC) is considered a suitable technology for leadless cardiac pacemaker applications, in terms of both power and size optimization. In this work, we suggest a power-optimized method for atrioventricular synchronization (AVS). First, we estimated the channel loss for intra-cardiac intra-body communication signals using quasi-static simulations. This was an essential study to define the specification limits of intra-body communication transceivers for atrioventricular synchronization. We then designed a superregenerative receiver (SRR) in 0.18 µm CMOS technology. The power consumption of the superregenerative receiver circuit was further optimized using a communication strategy for the atrioventricular synchronization application, achieving levels of power consumption as low as 340 nW. This study showed the feasibility of a telemetry-based synchronization of dual-chamber leadless cardiac pacemaker systems while minimizing the impact on the device's longevity.

1. Introduction

More than one million pacemakers are implanted every year worldwide to treat patients suffering from abnormally low heart rhythms, known as bradycardia. Conventional pacemakers consist of a subcutaneously implanted can integrating all the electronic components, and up to three leads to intravenously reach the heart's chambers (Figure 1). Nowadays, the battery density allows integrating all pacemaker functionalities into small capsules that can be directly fixed at the patient's endocardium. This kind of device is known as a leadless cardiac pacemaker (LCP). It was considered as a potentially groundbreaking innovation in the cardiac rhythm management (CRM) business.

One of the major benefits of the leadless cardiac pacemaker is the absence of a subcutaneous pocket and a reduction in foreign material, lowering the incidence of infection [1]. However, as standalone devices, leadless pacemakers can only be used for single-chamber therapies, limiting the eligible patient population. Future developments will likely allow the implantation of two or more leadless cardiac pacemakers to pace in a coordinated manner in different locations of the heart. In [2], Bereuter et al. proved the feasibility of multi-node leadless pacing using a conductive approach, intra-body communication (IBC), to synchronize the therapy among leadless cardiac pacemaker nodes. Intra-body communication is an ultra-low-power method of communication since no radiation is involved. It is well suited for leadless cardiac pacemaker application since no additional components are strictly required, such as antennae or inductive coils that are necessary for standard radiofrequency techniques. The intra-body communication signals are induced and sensed using electrodes. Indeed, an emitting pair of electrodes induces an electric field that

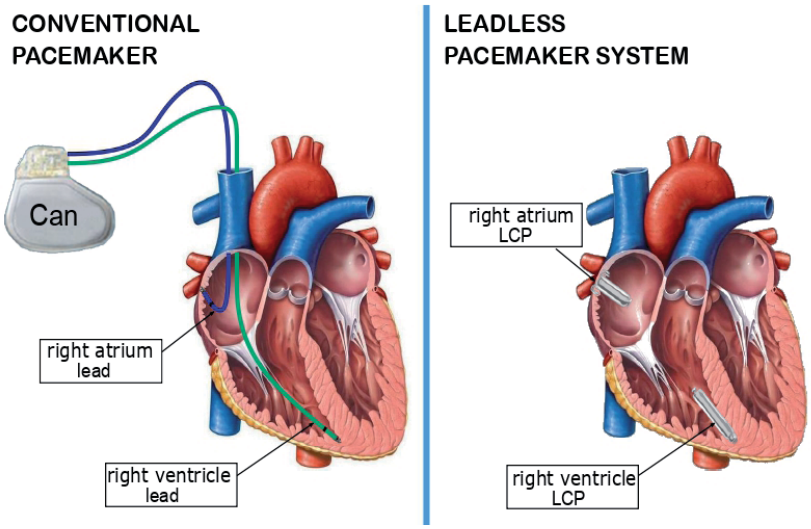

Figure 1. A representation of the conventional dual-chamber pacemaker (left) and the dual-chamber leadless pacemaker system (right)

propagates through the body's tissues reaching another electrode pair at the receiver side. Bereuter's work involved preliminary studies, leaving unaddressed several key aspects related to the system feasibility, such as the power consumption of the telemetry module.

In this work, we suggest a power-optimized design of a communication system for a leadless dual-chamber system. In Section 2, we present the simulation model we used to estimate the path loss of intra-body communication signals for the intra-cardiac channel. The path-loss estimation was essential to complete the specification limits for the intra-body communication transceiver, which are pointed out in Section 3. In Section 4, we introduce the superregenerative receiver (SRR), which is considered a suitable architecture to respect the transceiver constraints. The design of the superregenerative receiver, tailored for the leadless cardiac pacemaker synchronization, is then discussed in Section 5. We point out the main simulation results in Section 6. The management of the receiver's active time is discussed in Section 7, where a communication strategy is proposed to drastically reduce the duty cycle of the receiver, theoretically ensuring 100% of atrioventricular synchronization. In Section 8 we discuss the results, while in Section 9 we point out the conclusions arising from this study.

Figure 2. A torso CAD model imported into the *COMSOL* environment.

2. Channel Path-Loss Characterization

In this section, we report the preliminary study about the path-loss characterization for leadless cardiac pacemaker synchronization. In particular, this work points out the results of the intra-cardiac channel, which represents the communication link between two leadless cardiac pacemakers implanted in the right ventricle (RV) and the right atrium (RA).

2.1 Methods

We designed a torso model to estimate the path loss of intra-body communication signals involved in leadless cardiac pacemaker applications. The model was based on a validated human model retrieved by the CT scan imaging of a 34-year-old man, the *Duke* from *IT IS Foundation Zurich*, with a resolution of 0.5 mm and including all the internal organs. The geometrical model was imported in *COMSOL Multiphysics 5.3*, where it was enhanced to accurately resemble physiological characteristics such as

Figure 3. A cross-sectional cut of the torso CAD model passing through the ventricles. It is possible to distinguish the tissues considered for the simulation. From the outer to the inner: The connective tissue, the muscles, the sternum, the costal cartilage, the inflated lungs, the liver, and finally, the heart with its ventricles.

the size and volume of the chambers [3, 4]. The overall geometrical model is shown in Figure 2, whereas a cross-sectional image of a plane parallel to the base of the model is depicted in Figure 3. To estimate the attenuation levels of the intra-cardiac channel, two identical capsules, such as the one shown in Figure 4, were directly designed in *COMSOL*. They had a volume of 1 cm^3 , which is similar to the volume of leadless cardiac pacemaker capsules that are currently on the market [5]. The total length of the capsule was 33 mm, whereas the diameter of the can was equal to 6.4 mm. To minimize the attenuation across the propagation channel, it is common procedure in intra-body communication technology to maximize the distance between the electrodes and, consequently, the inter-electrode impedance [6]. To do so, we used the distal and the proximal electrodes that are pointed out in Figure 4. The capsules were placed respectively in the right ventricle and in the right atrium in positions commonly used for pacemaker leads. The right-ventricle capsule was fixed at the apex of the heart, whereas the right-atrium capsule was fixed at the anterior region of the lateral wall, known in the medical community as the free wall. Two different orientations were simulated to take into account the minimum and the maximum angle of the mutual orientation of the capsules. Both orientation scenarios had a channel distance of 9 cm, calculated as the distance between the median points of each capsule.

The torso was surrounded by a sphere of air with a radius equal to 0.6 m, the outer surface of which was set as an infinite boundary to avoid unwanted reflections of the electric field altering simulation results. The conductivity, σ , and relative permittivity, ε_r , of the biological tissues are frequency dependent [7], and were set using parametric functions with values acquired from Gabriel's studies [8].

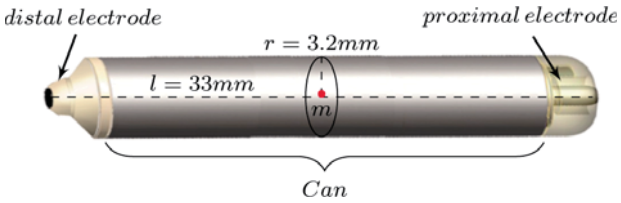

Figure 4. The leadless cardiac pacemaker prototype used for intra-body communication channel studies. The distal and proximal electrodes were spaced 33 mm apart. The can of the prototype had a diameter of 6.4 mm.

Simulations were performed using the *Electric Currents* interface of the *AC/DC* module that solves a current continuity equation problem using the Finite-Element Method (FEM) under quasi-static assumptions [9]. Two voltage boundary conditions were set on the emitting electrodes with equal absolute values and opposite polarity, $V_{TXi} = \pm 1.5$ V, whereas two surface boundary probes were defined at the receiving electrodes. The channel attenuation was calculated using Equation (1):

$$A_{\mathrm{dB}} = -20 \times \log \frac{|V_{RX1} - V_{RX2}|}{|V_{TX1} - V_{TX2}|}. \quad (1)$$

The whole model geometry was meshed with a custom tetrahedral meshing the minimum element size of which was set to 50 μm in order to adapt mesh sizes to the local complexity of the model. The outer layer of the air sphere was meshed using the swept meshing technique to accurately and efficiently mesh infinite boundary domains. The frequency range of interest was set between 40 kHz and 20 MHz. The lower bound of the frequency range was selected to ensure a margin with respect to electrophysiological signals, whereas the upper bound was set at the limit of the model according to quasi-static assumptions. In particular, the relative error of the electric-field amplitude due to the magnetic-field contribution can be estimated using [10]

$$\frac{E_{error}}{E} = \omega^2 \mu \varepsilon r_{tx}^2, \quad (2)$$

where ω is the angular frequency, r_{tx} is the dipole length of the emitter in meters, and μ and ε are respectively the magnetic permeability and the electric permittivity of the medium. Knowing that $\mu_{tissue} \approx \mu_{air}$ and ε_{blood} (20 MHz) = 154.56, we found a relative error of almost 3% , which could be considered an acceptable limit.

2.2 Results

The mutual orientation between emitter and receiver is very effective in galvanic intra-body communication. However, the right atrium capsule must be placed to optimize the response to therapy stimulation rather than improving the

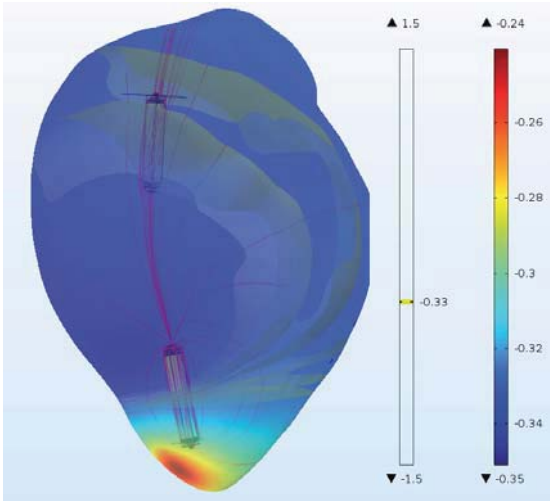

Figure 5a. The position of the right-atrium capsule for the best case. The electric-field lines are represented in red, whereas iso-potential surfaces are represented in green. Five iso-potential surfaces were plotted, where each subsequent iso-surface differed by 2 mV from the previous one.

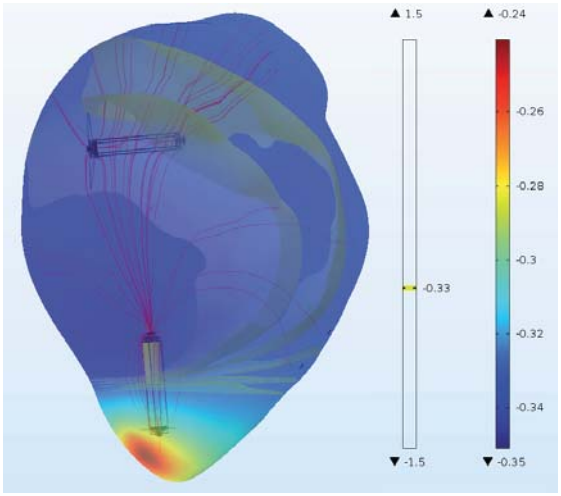

Figure 5b. The position of the right-atrium capsule for the worst case. The description from Figure 5a applies.

communication link among devices. It is hence important to characterize both best- and worst-case positioning of the right atrium capsule. In the best-case scenario, the electric-field lines are aligned with the receiver capsule, as seen in Figure 5a, which yields a higher differential voltage across the receiving dipole. For the same reason, the worst-case scenario would arise when capsules are orthogonal to each other, Figure 5b. The intra-cardiac simulation results are shown in Figure 6, where the difference between the worst and best case was $\sim$11 dB. In both scenarios, the attenuation decreased by $\sim$5 dB from 40 kHz to 20 MHz.

An exhaustive study of all the channels involved in leadless cardiac pacemaker applications was reported in [24], including the validation of the simulation model through in-vitro and in-vivo measurements. The attenuation levels of the intra-cardiac channel do not preclude any frequencies being used for leadless cardiac pacemaker synchronization. The carrier frequency can thus be selected according to design constraints that will be dealt with in the following sections.

3. Transceiver Specifications

In this section, we point out the maximum specifications of the intra-body communication transceivers for the synchronization of leadless pacemakers.

3.1 Average Current Consumption

Leadless cardiac pacemakers are limited in size, reducing the battery capacity, which ranges from 120 mAh to 248 mAh, and they generally have a nominal voltage equal to 3.3 V [5]. Nevertheless, leadless cardiac pacemaker lifetime must be ensured for several years to minimize the number of surgical operations required to replace the exhausted device with a new one. Let us evaluate the average current budget leading to a device longevity of 10 years. To do so, it is possible to calculate the average current consumption range of the whole device as

$$I_{average} = \frac{battery\ capacity}{10\ years} \approx [1.37 - 2.83]\ \mu A. \qquad (3)$$

To minimize the impact of the communication module on the device's longevity, we can set the average current consumption of the transceiver, I_{COM}, one order of magnitude lower than $I_{average}$, leading to values as low as hundreds of nA referenced to the nominal voltage of the battery, 3.3 V.

3.2 Latency

As a gold standard, physicians measure heart-chamber synchrony through Doppler echocardiography, and tune the pacing delay of the ventricles with respect to the atrial activity. In the optimal delay condition, the cardiac output – which is the volume of the blood ejected from the heart – is maximized. This optimal condition is referred to as atrioventricular synchrony. Manufacturers of echocardiography systems provide time resolution of the order of 10 ms [25]. From a clinical-validation point of view, atrioventricular synchronization (AVS) can thus have at most the same time resolution of echocardiography measurements. Consequently, the latency – defined as the delay between the detection of the atrial activity in the right atrium and the demodulation of the synchronization message in the right ventricle capsule – must not exceed 10 ms.

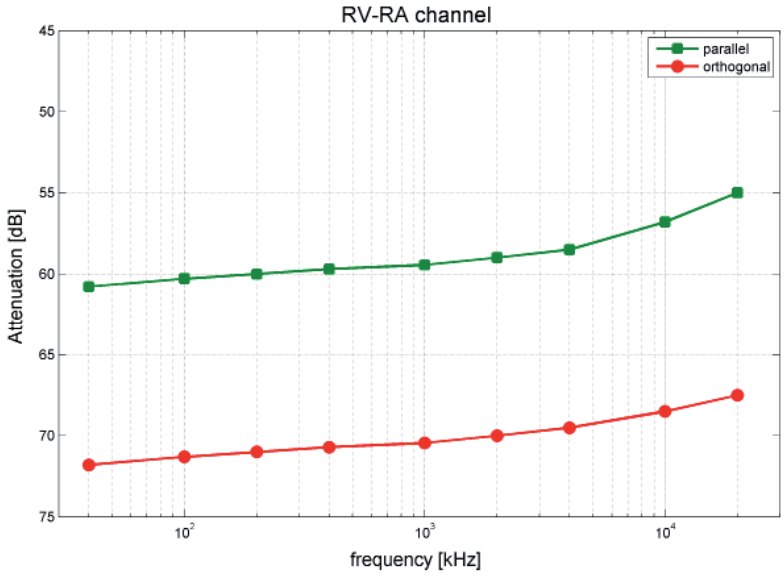

Figure 6. The attenuation levels of the intra-cardiac channel (RVRA) for the best-case (green line) and worst-case (red line) positioning of the right-atrium capsule

3.3 Maximum Emitting Voltage and Sensitivity

Leadless cardiac pacemakers must respect emission limits to ensure safety for patients. The International Commission on Non-Ionizing Radiation Protection (ICNIRP) provides safety guidelines for radiation exposure over a broad frequency spectrum. For what concerns the high-frequency spectrum (HF), the physical quantities used to measure radiation exposure are the Specific Absorption Rate (SAR) and the current density. A numerical evaluation was conducted in [13], where the result suggested that it is not difficult to satisfy the SAR guidelines for Intra-Body Communication. Indeed, the authors obtained SAR levels 60 dB lower than the safety limit when they applied 1 V at the emitter side. Concerning the current-density restriction, the limit of its root-mean-square value is dependent on frequency. Specifically, the current-density limit was chosen to neglect the influence of transmitted signals to neuronal activity [14], and it was equal to

$$J = \frac{f}{100}\left[\mathrm{mA/m^2}\right], \tag{4}$$

where f is the frequency in Hz. It is not straightforward to comply with the current-density constraint since leadless cardiac pacemaker electrodes can be small in size, reaching considerable current-density levels. Considering an electrode having a contact surface $S = 4\ \mathrm{mm}^2$, and an inter-electrode impedance $R_e = 1\ \mathrm{k\Omega}$, we found that the current density was equal to

$$J = \frac{V_{RMS}}{SR_e} = \frac{250V_{RMS}}{1\Omega}. \tag{5}$$

Substituting this value into Equation (4), we found that the maximum voltage at the emitting capsule must be lower than

$$V_{RMS} = \frac{f}{25000}\ [\mathrm{V}]. \tag{6}$$

Knowing that the intra-body communication channel attenuation for dual-chamber leadless cardiac pacemaker systems can reach ~ -70 dB (Figure 6), we could set the sensitivity of the receiver to be

$$v_{in,RMS}\left[\min\right] = \frac{f}{25000}\times 10^{-\frac{70}{20}} = 4f\times 10^{-8.5}. \tag{7}$$

It was therefore convenient to maximize the carrier frequency of the signals to relax the sensitivity constraint.

3.4 Modulation

Since the main goal was to optimize transceiver power consumption, the modulation complexity had to be maintained as low as possible to relax transceiver performance requirements. On-off keying (OOK) and frequency-shift keying (FSK) are viable modulation schemes for ultra-low-power applications. In general, frequency-shift keying modulation requires more power

at the receiver side compared to on-off-keying-modulated signals, due to the necessity for an internal frequency reference to demodulate incoming signals [15]. Frequency-shift-keying receivers usually experience higher bit rates compared to on-off-keying receivers. However, the leadless cardiac pacemaker synchronization does not require high-data-rate communications. Considering that the latency constraint is respected, the cardiac-event message reduces to binary information, allowing the communication module to work with a single-bit demodulation. We thus suggested the on-off-keying modulation rather than the frequency-shift keying to reduce the complexity of the communication system.

3.5 Bit Error Rate (BER)

For atrioventricular synchronization applications, the information that we need to share among different leadless cardiac pacemakers is related to the electrical activation of the heart. We thus could design the receiver to neglect the probability of the communication loss compared to the error probability of ECG sensors. The sensors could miss atrial events for several reasons: pacemaker programming problems (improper sensing threshold), insufficient myocardial voltage signal, pacer failure (fibrosis), or an electrolyte abnormality [16, 17]. The most trivial sensing concerns atrial activations. Loss of atrial sensing is 2%-11% among patients of clinical studies reported in the literature [18]. The error probability of the communication must thus be at least ten times lower than the probability of missing atrial detection, leading to a BER of 10^{-3} for single-bit synchronization signals. The error probability of on-off-keying signals is well approximated by the function

$$P_e = Q\left(\sqrt{2SNR}\right), \tag{8}$$

where Q is the Q function, the distribution of which depends on the signal-noise ratio, SNR [19]. According to Equation (8), the SNR must be greater than or equal to 10 dB to achieve a BER of 10^{-3}. Recalling that the input signal amplitude can be as low as –84 dBV and considering a margin of at least 10 dB for the receiver noise figure (NF), the maximum input noise amplitude must be lower than –104 dBV.

The intra-body communication channel can be considered as an additive white Gaussian noise channel (AWGN). Under this assumption, we could model the thermal noise of the inter-electrode resistance as a voltage source, the spectral density of which is

$$N_0 = \sqrt{4K_B T\, R\, BW}\,, \tag{9}$$

where K_B is the Boltzmann constant, T is the temperature in kelvin, R is the inter-electrode resistance, and BW is the bandwidth of interest. Considering that the body temperature is approximately 37°C (310.15 K) for $R = 1\ \mathrm{k\Omega}$, the spectral noise density is

$$N_0 = 4.13\ \mathrm{nV}/\sqrt{\mathrm{Hz}} = -166.65\ \mathrm{dBV}/\sqrt{\mathrm{Hz}}\,. \tag{10}$$

Classically, the input resistance of the receiver is matched with the equivalent source resistance to minimize the input noise of the receiver. To maximize the useful input voltage of the receiver for the intra-cardiac channel, the input resistance of the receiver must here be much greater than the equivalent inter-electrode resistance [11]. The input noise can thus be considered equal to the thermal noise of the inter-electrode resistance.

The synchronization signal, $s(t)$, can be interpreted as a train of pulses with period equal to the cardiac cycle, T_{CC}, and pulse duration equal to T_{bit}. We could assume that T_{CC} is infinitely longer than T_{bit}, allowing the time-analysis of the signal to be reduced to a single pulse. Considering only the first harmonic of the carrier, the synchronization pulse can then be represented in the time domain as

$$s(t) = \prod_{\frac{T_{bit}}{2}} \cos\left(2\pi f_0 t\right), \tag{11}$$

where Π is the rectangular function, t is the time variable, and f_0 is the carrier-frequency value. Applying the convolution theorem of the Fourier transform, we can easily retrieve the analytical representation of synchronization pulse in the positive frequency domain:

$$S(f) = T_{bit}\,\mathrm{Sinc}\left(\pi f T_{bit}\right) * \delta\left(f - f_0\right). \tag{12}$$

We could reasonably approximate the bandwidth of the synchronization signal to the main lobe of $S(f)$ that is equal to $4\frac{1}{T_{bit}}$. As a result, we found the maximum allowed bandwidth of the synchronization signal to be

$$\sqrt{BW}\,N_0 \le -104\,\mathrm{dBV} \Rightarrow BW = 4\ \mathrm{THz}\,. \tag{13}$$

Recalling the relationship between the bit duration and bandwidth of the on-off-keying-modulated synchronization signal, we found a minimum bit duration of $T_{bit} = 1\,\mathrm{ps}$, which is far shorter than the needs of this application.

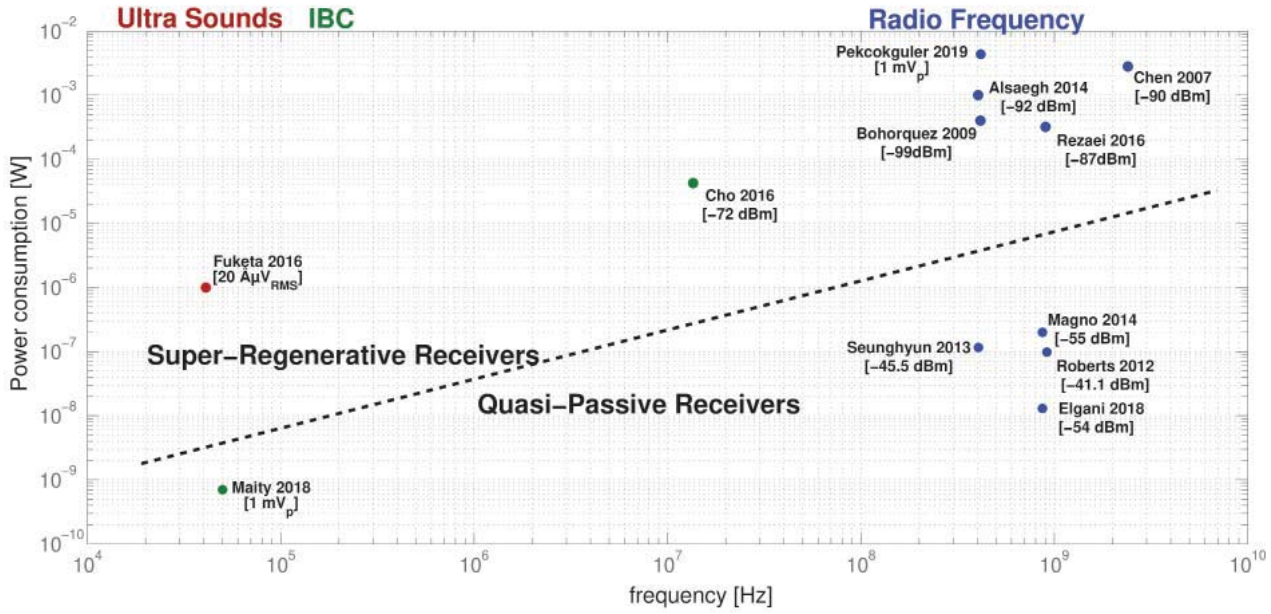

Figure 7. The power consumption of ultra-low-power on-off-keying receivers over a wide spectrum ranges.

4. Receiver Architecture

4.1 Main Ultra-Low-Power Topologies

In this section, we point out two families of on-off-keying receiver known for minimizing the power consumption: the quasi-passive and the superregenerative receivers.

In the last decade, several quasi-passive wakeup receivers have been proposed [20-24]. Those solutions relied on signal-rectification techniques widely used for wireless power transfer [25]. This method is suited for reaching power-consumption values in the sub-micro-Watt scale. By the way, on-off-keying receivers usually have low sensitivity, due to diode-threshold-voltage activation.

An elegant approach to minimizing power consumption while increasing the sensitivity of on-off-keying receivers comes from the superregenerative architecture. The superregenerative receiver (SRR) has been widely used in the literature for ultra-low-power applications, since only two high-frequency blocks are required to demodulate on-off-keying signals [26]. The superregenerative receiver architecture can be used on the whole frequency spectrum and with different physical waves. In [27], Fuketa designed a superregenerative receiver in 0.25 µm technology for ultrasound communication using an external transducer to couple the front-end LNA of the receiver. Superregenerative receivers for medical applications in the MICS band were proposed in [28-30], whereas receiver designs for the ISM band were suggested in [31] and [32], with center frequencies respectively at 900 MHz and 2.4 GHz. A low-power solution for intra-body communication for body-surface applications was also provided in [33] using a carrier frequency of 13.56 MHz. Figure 7 is a log-scale plot that summarizes the performance of all reported on-off-keying receivers, where we can see a linear dependence of the power consumption on frequency. High sensitivity values are reachable over the whole frequency spectrum thanks to the high gain of the superregenerative receiver's architecture. Indeed, it is possible to achieve extremely high gains and narrow-band filtering with a limited amount of current consumption thanks to the superregenerative receiver's architecture.

4.2 The Superregenerative Receiver

As pointed out in Figure 8, the core of the superregenerative receiver is an oscillator (SRO) the feedback amplifier of which has a time-dependent gain. Above a critical gain value, the oscillator is able to satisfy the first Barkhausen criterion [34], leading to oscillation to occur. A control signal drives the time-evolution of the gain to periodically counteract the oscillator dispersion. As a result, the system alternates unstable periods, where oscillations occur, and damping periods, where the control signal quenches the oscillations. The resonant tank circuit that fixes the resonance frequency of the oscillator is coupled with the input signal, v_{in} . The response of the oscillator thus varies according to the amplitude and the frequency of v_{in} . The second active device required by the superregenerative receiver is the low-noise transconductance amplifier (LNTA) at the front-end of the receiver. The low-noise transconductance amplifier has a dual function: it injects in the oscillator tank an amount of current that is proportional to the amplitude of the input signal, and it isolates the input interface reducing the leakage that would cause

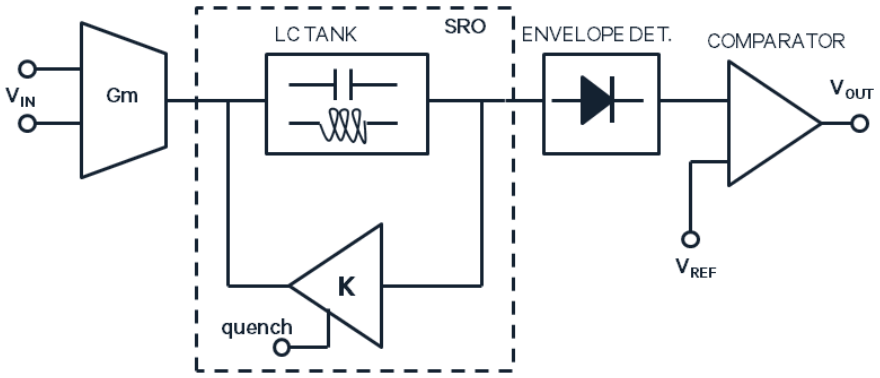

Figure 8. A block schematic of a superregenerative receiver.

involuntary emissions when the system is resonating. Finally, the baseband information is retrieved by comparing the envelope of the output of the oscillator to a threshold value, V_{REF} . As a result, the superregenerative receiver is a sampling system with extremely high gain, the maximum data rate of which is limited by the quenching frequency.

5. Circuit Design

The whole receiver was designed using a 0.18 μm CMOS technology, since this can also handle high-voltage applications, allowing the integration of all leadless cardiac pacemaker functionalities in a single chip to reduce the fabrication costs of the device.

For the core of our superregenerative receiver, we decided on adopting the *Pierce oscillator* topology to minimize the number of inductive components. Due to the limited working frequency of intra-body communication, the chip integration of the inductance would be unreasonable in terms of size and, consequently, production costs. We thus could use an external inductor for the selective network. We chose the SDR0302-820KL since this component was a good compromise between high inductance and size. The resonance frequency of the selective network was set to 4 MHz as a compromise between inductance stability and sensitivity requirement. The capacitors of the selective network, C_1 and C_2 , were integrated on chip with capacitances respectively equal to 28.97 pF and 58 pF. Furthermore, the value of C_1 was trimmed with an 11-bit precision. The trimming of C_1 was necessary to calibrate the resonating frequency to the selected carrier frequency of 4 MHz, considering the tolerance of the inductor and the process variations. To avoid the equivalent resistances of the superregenerative receiver blocks degrading the oscillatory response of the tank, we integrated three decoupling capacitors, C_{d1} , C_{d2} , and C_{d3} , the values of which were selected to behave as a short circuit at the resonance frequency.

Thanks to the low data rate required by this application, we could relax the constraint on the quenching frequency. To minimize both power consumption and chip size, we decided to build the quench signal using the 32 kHz clock of the leadless cardiac pacemaker. The feedback amplifier of the oscillator was the common-source amplifier, M_1 . As such, the gain of the feedback amplifier could be driven by controlling the drain current of

$$A(I_D) = -g_m r_{out}(I_D).$$

The quench signal had to slowly change to improve the sensitivity of the superregenerative receiver. On the other hand, the quenching had to ensure full depletion of the charges stored in the tank to avoid inter-symbol interference. To reduce the quench period, we suggested separately facing the dual task of the quench signal.

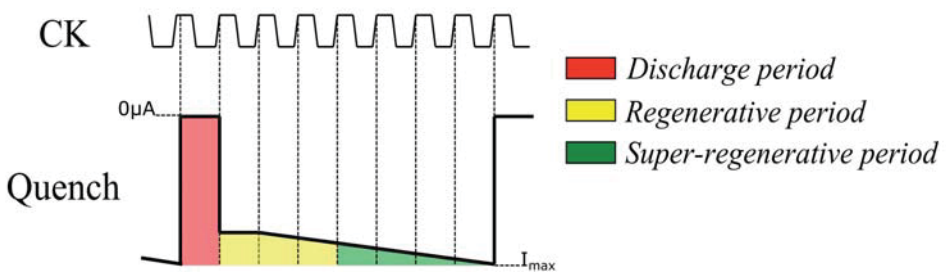

Figure 9. The time evolution of the quenching signal.

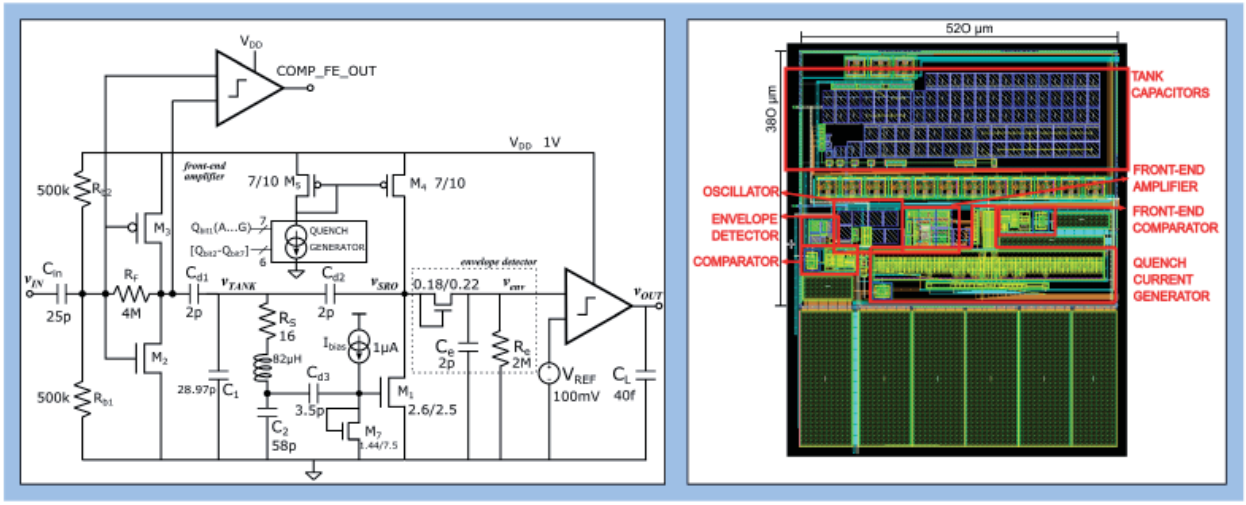

Figure 10. The schematic (left) and layout (right) of the superregenerative receiver proposed in this work.

Figure 9 shows the suggested waveform used to quench the oscillator. It consisted of a clock-driven signal that we could qualitatively divide into three regions:

- The discharge period used to deplete the capacitors of the tank circuit;
- The regenerative period used to initially charge the tank circuit according to the input signal coming from the front-end circuit;
- The superregenerative period, where the oscillator was unstable, boosting the amplitude of the injected signal through the oscillatory response.

The whole quench signal spread over eight clock cycles, leading to a quenching period $T_{quench} = 250$ µs. The discharge period lasted for one clock cycle and it was characterized by abrupt variations, leading to a fast discharge of the selective circuit. During the second clock cycle, the quench signal passed from the discharge period to the regenerative period. Here, the current drawn to the amplifier was not sufficient to satisfy the gain condition of the oscillator, but it was high enough to neglect the damping of the injected signal.

Once the quench waveform was decided, we designed the quench generator as a network of current mirrors, with different ratios converging on the same node. Each branch of the quench generator was enabled by a CMOS switch to control the initial quench current, I_{start}, and the quenching period. In particular, seven bits were used to calibrate I_{start}, whereas six bits were used to sequentially increase the quench current with a constant step of 30 nA during the superregenerative period. As a result, we had a programmable current sink in terms of amplitude and quenching period. The p-MOS pair M4-M5 mirrored the quenching current to bias the common-source amplifier, M_1. Monte Carlo simulations showed a maximum offset of 350 nA of the initial condition of the quenching current, which could be easily compensated through the seven-bit trimming circuit.

At the front end, the transconductance amplifier was designed as a CMOS inverter biased in the transition region, where a resistive feedback was used to better fix the bias point stabilizing the gain [35]. The inverter topology led to a small area dimension and low complexity for single-ended amplifiers. Moreover, it allowed rail-to-rail operations with reduced supply voltage levels, which was an interesting characteristic for ultra-low-power applications.

To maximize the value of the feedback resistance, we designed a matched inverter-amplifier such that in typical conditions, $V_{in} = V_{out} \approx \frac{V_{DD}}{2}$. However, process variations could change the bias point of the amplifier and make it work out of the transition region, where it would behave as a classic inverter. To counteract this effect, the input bias resistors, R_{b1} and R_{b2}, were trimmed over eight bits. A second comparator was used to sense the bias point of the front-end amplifier and give a digital feedback to find the right combination for the trimmed network.

The output resistance of the inverter was designed to be much greater than the oscillator resistance, such that the oscillator gain was independent of the front-end circuitry. The transconductance of the amplifier, G_m, was set to 200 µS, leading to an overall gain at the resonance frequency equal to

$$A_v(j\omega_0) = -G_m Z_L(j\omega_0) \approx 22.5 \text{ dB}. \quad (14)$$

To retrieve the envelope of the oscillator (SRO) output, we used a passive rectifier circuit [25]. We decided to use an MOS diode with minimum size to maximize its resistance and minimize the occupied area. The pole related to the time constant of the envelope detector was set to 40 kHz to let the envelope of the signal pass and minimize the ripples at the resonating frequency.

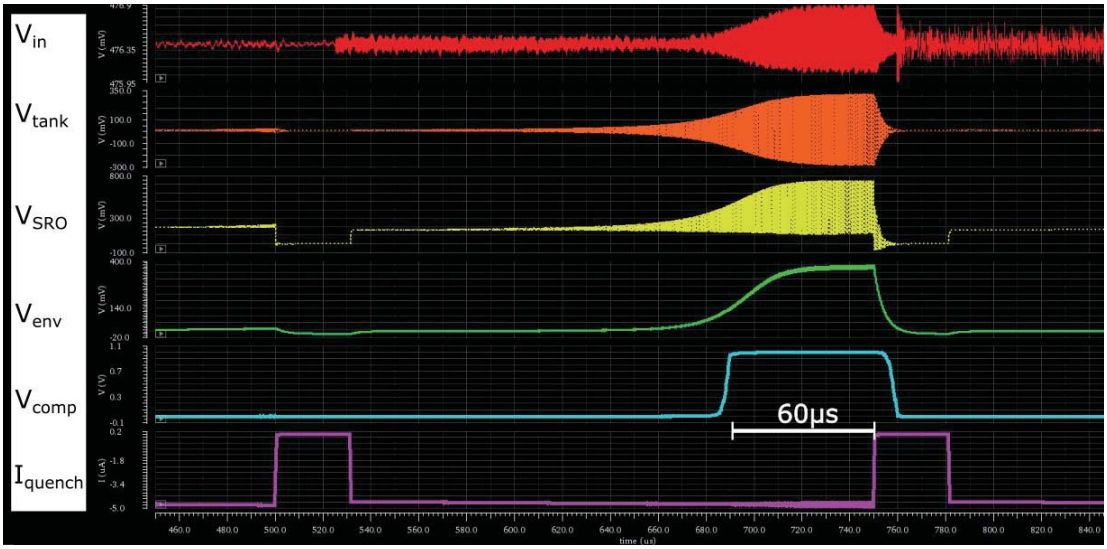

Figure 11. The time evolution of the input signal through the proposed superregenerative receiver.

For the comparator, we used a self-biased architecture [36]. The main advantage of this topology was that the circuit could source and sink high values of current with low quiescent consumption. We thus could have a fast response with low power consumption.

The schematic diagram and layout of the superregnerative receiver are shown in Figure 10.

6. Superregenerative Receiver Simulation Results

Figure 11 shows the evolution of the on-off keying signal through the circuit. All the simulations performed included the thermal noise of the components to discriminate eventually false detections. The peak amplitude of the input signal was set to 90 µV. The input level followed the oscillating response of the resonant circuit; however, the voltage levels were moderate, reaching a peak-to-peak voltage level of 700 µV. The voltage across the tank circuit (V_TANK) was an oscillating sinusoid that reached saturation for a peak level of 300 mV with an almost null dc component. The maximum limit of V_TANK came from the output dynamic of the superregenerative oscillator: as could be seen, the signal SRO_OUT had the same peak-to-peak level as V_TANK. As soon as the oscillations rose, the voltage across the load of the envelope detector increased, reaching its maximum at 380 mV. This voltage level came from the peak voltage of the oscillator output and a residual contribution of the time-varying dc point of the oscillator output. The output of the comparator (OUT_COMP) converted the low dynamic of SRO_OUT into a signal that was detectable by the binary logic of the digital circuit. The current signal of Figure 11 represents the quenching signal of the oscillator. The internal clock of the device drove the quenching current of the oscillator, as previously described. The output signal of the receiver rose almost 60 µs before the end of the quench cycle, allowing for relaxing the routing constraint of the clock signal to demodulate the information.

6.1 Sensitivity

Parametric simulations of the input voltage were used to find the sensitivity of the receiver. The minimum voltage amplitude that was detectable by the receiver was about 10 µV. However, the time margin between the end of the quench cycle and the rise of the output signal lowered to 2 µs. The proposed receiver circuitry respected the high-sensitivity property of the superregenerative receiver's architecture. At first glance, the receiver might not have seemed power optimized concerning the sensitivity required. However, it is worth pointing out that this was the reference simulation performed with typical parameters of the MOS transistors at 37°C, which is the average body temperature. The minimum sensitivity was ensured over a broader temperature range (27°C to 50°C).

6.2 Bit Error Rate

The input signal was modeled as an on-off keying signal with a fixed pulse width and a variable period. The period was modeled as a stochastic variable with a Gaussian distribution centered at $\mu = 3.33$ ms with a variance $\sigma^2 = 0.08\mu$. The variance was selected to limit the input period variation to 25%, according to the maximum

Table 1. Power consumption distribution.

Receiver Block	I_{RMS}	V_{DD}	Active Power
LNTA	8.7 µA	1 V	8.7 µW
SRO	9.5 µA	1 V	9.5 µW
Comparator	28 nA	1 V	28 nW

acceleration of the sinoatrial activity. The mean value of the Gaussian distribution, μ, was selected to have a reasonable computational time, estimated to 24 hours. We performed a transient simulation of 34 s, leading to a number of pulses

$$n \approx \frac{T_{sim}}{T_s} = \frac{34\,\text{s}}{3.333\,\text{ms}} \approx 10^4. \quad (15)$$

The results of the simulation experienced no missing detections, ensuring a BER lower than 10^{-4}, which was already ten times better than the specification requirements. Moreover, no false detections were experienced, as well.

6.3 Power Consumption

The supply voltage of the receiver was fixed and equal to 1 V. On the other hand, the current varied over time due to the current-driven quenching of the oscillator. The active power consumption of the proposed circuit thus could be found as

$$P_{active} = V_{supply} I_{RMS} = 18.25\,\mu\text{W}, \quad (16)$$

where I_{RMS} is the root-mean-square current drawn by the supply-voltage generator. In Table 1, the distribution of the active power consumption among the blocks of the proposed receiver is reported.

As shown in Table 1, the power consumption was dominated by the front-end amplifier and the oscillator, while the comparator's contribution was negligible, since it handled the baseband signal with a frequency that was several orders of magnitude lower than the carrier frequency. Even though the receiver was tailored to the application, the power consumption was still too high for continuous functioning. In the next section, we describe a communication strategy for the atrioventricular synchronization of dual-chamber leadless cardiac pacemakers that optimizes the duty cycle of the receiver to achieve an average power consumption in the sub-micro-Watt domain.

7. Communication Strategy

In a healthy heart, the electrphysiological impulse that drives the heart beating arises from the sinoatrial node of the right atrium to the ventricles across specific conduction patterns of the heart's tissue. However, electrical dysfunctions of the conduction system can cause asynchrony to rise. Asynchrony among atrial and ventricular activity makes the heart's pumping less effective. Dual-chamber pacemakers counteract the asynchrony between the right atrium and the right ventricle by adapting the timing of the right-ventricle stimulation to the electrical activity of the right atrium, known as the P-wave for the ECG nomenclature.

The capsule implanted in the right ventricle requires the atrial activity information, such as the P-event detection of ECG sensors, to artificially synchronize the ventricular activity. The communication protocol is driven by the right-atrium capsule, which sends a synchronization pulse to the right ventricle as soon as the P-wave detection occurs. To ensure a correct transmission of the information, the pulse width of the synchronization signal is

$$T_{sync} = 2T_{quench} = 500\,\mu\text{s}, \quad (17)$$

where T_{quench} is the quenching period of the superregenerative receiver. We suggested an adaptive listening window that exploits the periodicity property of P-wave events. According to clinical studies [14], the physiological PP-interval does not accelerate by more than 25% to 35% from beat to beat.

The right-ventricle capsule stores the timing information of the synchronization pulse when it correctly receives it. In case of no detection, it sends a stimulation request to the right-atrium capsule. The timing of previous synchronization pulses can be used to estimate the next P-wave event. Recalling that the variability of physiological P-wave acceleration is $\sim 25\%$, we could reduce the listening window accordingly. In this condition, the average power consumption of the receiver was reduced by a factor of four, but it was still unreasonable compared to the total power budget of leadless cardiac pacemakers. Let us now divide the synchronization issue into two separate aspects: the duty-cycle reduction, and the communication-module synchronization.

7.1 Duty Cycle Optimization for AV Synchronization

Recalling that the leadless cardiac pacemaker synchronization must occur with a maximum latency of 10 ms, we could degrade the latency of the information transmission, reducing the duty cycle of the communication module. Assuming that the receiver was turned on for two quench periods, there were still 9.5 ms of margin for the demodulation latency. We proposed an event-driven communication that could occur during a predetermined period. The basic concept was to map the physiologic period where the P-wave could occur into periodic communication slots, where the communication could be enabled. It is worth reminding that the P-wave acceleration is relative to the real-time heart rate. The number of communication slots thus must be adapted to the heart rate as well. The time-window was composed of n periodic slots, covering the whole physiological time-window for both the emitter (right-atrium capsule) and the receiver (right-ventricle capsule).

Let us first consider the emitting slots of the right-atrium capsule. Each slot was equally spaced in time by T_{slot} and had duration pulse equal to T_{bit}. When the right-atrium capsule detected the P-wave, it used the first possible emitting slot of the TX window to send the synchronization pulse to the right-ventricle capsule. On the other hand, the right-ventricle capsule mapped the physiological time-window into the same number of communication slots, *n*. Each slot was composed of a SLEEP-period and an ON-period. During the SLEEP-period, the device turned off the receiver, whereas during the ON-period, it kept it active. The number of slots, *n*, was given as the first integer number coming from the ratio between the physiological P-wave time-window and a single sub-block period(T_{sub}):

$$n = \frac{T_{RX}}{T_{sub}} = \frac{25\% Heart\ Cycle}{T_{Sleep} + T_{ON}} \tag{18}$$

For example, if we considered having a heartbeat rate of 60 bpm, the total physiological period was equal to 250 ms. Setting $T_{sleep} = 9.5$ ms and $T_{ON} = 0.5$ ms led to $n = 25$, reducing the overall listening time to 12.5 ms.

7.2 Communication Window Synchronization

To ensure correct transmission of the synchronization pulse, the capsules had to have the same time reference, aligning the emitting and receiving slots. As we mentioned before, we suggested taking advantage of the periodic nature of physiological P-waves to adapt the communication slots.

Let us assume that the right-atrium capsule detected a P-event: it would use the first slot after the detection to send a synchronization pulse. In particular, the first synchronization pulse was used to initiate the communication strategy for both the right-atrium capsule and the right-ventricle capsule, setting to zero a reference timer. Let us define the value stored in the timers of the right-atrium and the right-ventricle capsules, respectively, as PP_{tx} and PP_{rx}. After initialization, the synchronization pulses were used to couple the right-ventricle capsule stimulation to the atrial activity. Figure 12 gives a graphical representation of the protocol for the P-wave transmission, where the right-atrium capsule sent an on-off keying-modulated pulse with duration T_{bit}, whereas the right-ventricle capsule sensed the presence of the synchronization pulse through the superregenerative receiver.

The right-atrium capsule stored the value of its reference timer, PP_{tx}, at the end of the transmission of the synchronization pulse. The right-atrium capsule used PP_{tx} to calculate the starting time of the TX window for the next heart cycle ($t_{Pest,RA}$).

During the first heart cycle, the right-ventricle capsule had no clue about whether and when the synchronization pulse could occur. The receiver was thus active all the time in a continuous way. As soon as the right-ventricle capsule detected the first synchronization pulse, it stored the value of its reference timer, PP_{rx}. As a result, the time correlation between reference timers of the capsules was given by

$$PP_{tx,i} = PP_{rx,i} + (\Delta t_i - T_{bit}), \tag{19}$$

where Δt_i is the demodulation delay of the superregenerative receiver for the *i*th atrial event, which is strictly positive by

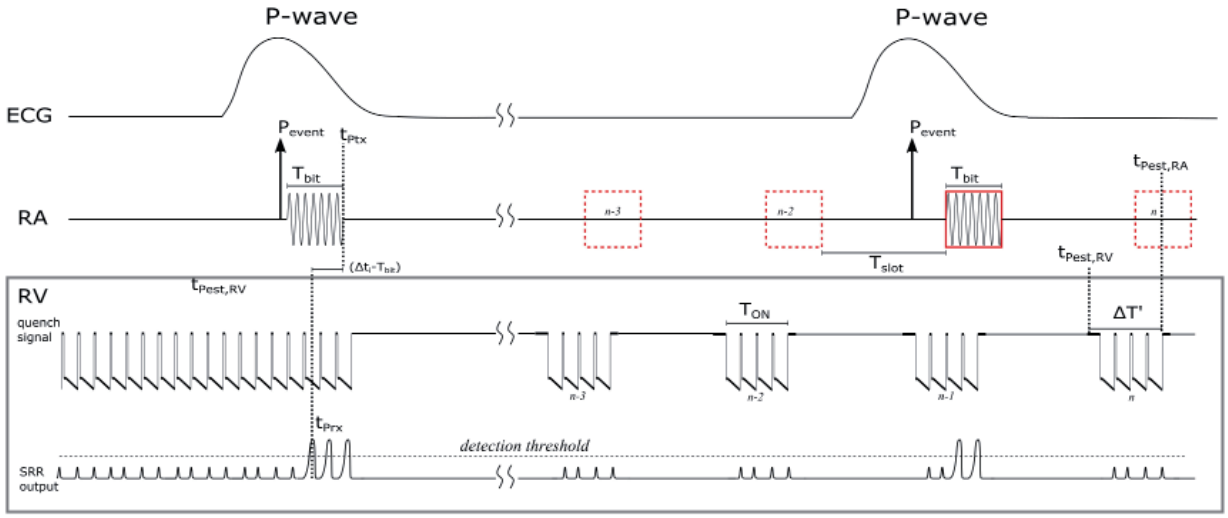

Figure 12. The transmission of the P-wave detection from the right-atrium capsule to the right-ventricle capsule, using the superregenerative receiver. The figures highlight the passage from an asynchronous transmission to a referenced transmission for atrio-ventricular synchronization.

Table 2. Performance of the designed receiver.

Parameter	Cho2016	This Work
Technology	65 nm	180 nm
Supply voltage	0.8 V	1 V
Frequency	13.56 MHz	4 MHz
Latency	10 µs	250 µs
Modulation	OOK	OOK
Data rate	100 kbps	2 kbps
BER	10^{-5}	$< 10^{-4}$
Sensitivity	1 µV	10 µV
Power consumption	42.5 µW	18.25 µW

definition. In particular, the value of Δt_i will depend on the amplitude of the incoming signal, but at least it takes t_0 clock cycles to reach the saturation of the superregenerative receiver. We thus could assume that

$$64\ \mu s < \Delta t_i < 250\ \mu s. \tag{20}$$

Now, we could use the values of PP_{tx} and PP_{rx} as the P-event expectation to define the communication slots discussed in the previous subsection. We could center the nth slots to the expected P-event timing. If we set $T_{ON} = T_{bit} = 500\ \mu s$, we could cover the whole physiological window, ensuring superposition of the emitting and receiving slots for at least one quench cycle of the superregenerative receiver.

8. Discussion

With this work, we proposed a communication system for atrio-ventricular synchronization of multi-node leadless pacemaker systems using intra-body communication signals. The communication module was tailored on the atrioventricular synchronization application, starting from a preliminary analysis of the attenuation levels of intra-cardiac intra-body communication signals. We then performed a quantitative analysis of the maximum acceptable specification of on-off-keying transceivers able to accomplish leadless cardiac pacemaker synchronization. The most stringent constraint was the emitting voltage aiming to prevent interference with physiological neuronal activity. The higher the frequency, the lower the danger of perturbing the nervous system conduction. We thus suggested working in the MHz range.

We designed and simulated a superregenerative receiver in 0.18 µm CMOS technology tailored for synchronization purposes.

It is not possible to exhaustively compare the suggested receiver to similar receivers of the state of the art due to the lack of scientific work in the literature. We qualitatively compare this work with the superregenerative receiver proposed by Cho in Table 2. Even though the receivers differed in several characteristics, the comparison can give a qualitative representation of the scientific results of our work. The main achievement of our design was the active power consumption, which was less than half the power of the circuit proposed by Cho. This result was obtained by relaxing the constraints over data rate and sensitivity. It is worth pointing out that the maximum sensitivity of the receiver was still one order of magnitude lower than the worst-case input amplitude.

Quantitatively speaking, the receiver consumed about 18 µW, which was two orders of magnitude higher than the maximum power budget allowed for the communication module. We thus suggested a simple solution to reduce the average power consumption down to 1.25% of its active power. The stochastic nature of the physiologic P-wave does depend on its previous value. In particular, PP-intervals should not exceed a beat-to-beat acceleration of 25% to 35%. Here, we have considered limiting the maximum acceleration to 25%. However, it is possible to have a programmable limit with a slight increase in digital-circuit complexity. For the sake of simplicity, we limited the consideration only to positive accelerations, but the same approach could be used for deceleration of the P-wave, if required.

The proposed algorithm tracked previous PP-intervals to map sub-windows over the whole physiological variability period. Thanks to this method, we could synchronize heart chambers in a power-efficient way. The active power consumption adapted to the heart rate, making the average power consumption constant over time.

Thanks to the reduction of the duty cycle, the receiver could achieve an average power consumption as low as 320 nW for a P-wave variability of 35%. To guarantee the same longevity of a single-chamber leadless cardiac pacemaker – for example, 10 years – we would need an additive charge equal to

$$Q_{(\mathrm{mAh})} = \frac{I_{av} V_{DD}}{V_{bat}} 10\ \text{years} \approx 8.5\ \mathrm{mAh}\ . \tag{21}$$

The effort of this increase in battery capacity was rewarded with a continuous-time AV-synchrony, improving the hemodynamics of patients.

9. Conclusion

In this work, we addressed all the technological challenges for the telemetry of multi-node leadless pacemaker systems, pointing out the communication system requirements. A nice solution for the expected low-input signal levels came from the superregenerative receiver. The superregenerative receiver was particularly appealing

since it could achieve extremely high gains with the lowest number of high-frequency blocks. A superregenerative receiver was designed in 0.18 µm CMOS technology. The receiver was tailored for the synchronization of leadless cardiac pacemakers, achieving 18 µW of estimated active power. Simulation studies showed a robust design against noise, achieving a bit error rate lower than 0.01% of events with a sensitivity of −100 dBV.

Nevertheless, the active power consumption of the receiver prevented the leadless cardiac pacemaker from continuously listening to the communication channel. We thus acted on the optimization of the listening time of the receiver to reduce its impact on the device longevity. We proposed an adaptive communication strategy allowing the reduction of the receiver's duty cycle. As a result, we had a receiver that could detect a synchronization pulse at each cardiac cycle, consuming only 320 nW of the leadless cardiac pacemaker's power budget. The additional power required by the receiver could be compensated over ten years by increasing the battery-charge capacity by 8.5 mAh, which was approximately 14% of the total capacity of the smallest battery integrated into the leadless cardiac pacemakers currently on the market.

This system was optimized in leadless cardiac pacemaker capsules with a length equal to 33 mm; however, a simulation model proposed in this work could allow identifications of the attenuation levels for different capsule sizes. This is an important consideration to take into account because of the impact of the dipole's length on the intra-body communication signal's attenuation. This work led to the first power-optimized solution for communication-based leadless cardiac pacemaker synchronization.

10. Acknowledgement

This work was funded by the European Union's H2020:MSCA:ITN program for the "Wireless In-Body Environment Communication - WiBEC" project under the grant agreement No. 675353. We would like to acknowledge URSI-France, which nominated our work among the best PhD in radio -science of the year 2021 (https://www.ursi-france.org/ursi-france/prix-de-these-en-radiosciences; https://www.ursi-france.org/ursi-france/prix-de-these-en-radiosciences).

11. References

1. A. Kroman, B. Saour, and J. M. Prutkin, "Leadless Pacemakers: Recent and Future Developments," *Current Treatment Options in Cardiovascular Medicine*, **21**, 10, 2019, p. 54.

2. L. Bereuter, M. Gysin, T. Kueffer, M. Kucera, T. Niederhauser, J. Fuhrer, P. Heinisch, A. Zurbuchen, D. Obrist, H. Tanner, et al., "Leadless Dual-Chamber Pacing: A Novel Communication Method for Wireless Pacemaker Synchronization," *JACC: Basic to Translational Science*, **3**, 6, 2018, pp. 813-823.

3. A. M. Maceira, S. K. Prasad, M. Khan, and D. J. Pennell, "Reference Right Ventricular Systolic and Diastolic Function Normalized to Age, Gender and Body Surface Area From Steady-State Free Precession Cardiovascular Magnetic Resonance," *European Heart Journal*, **27**, 23, 2006, pp. 2879-2888.

4. Y. Wang, J. M. Gutman, D. Heilbron, D. Wahr, and N. B. Schiller, "Atrial Volume in a Normal Adult Population by Two-Dimensional Echocardiography," *Chest*, **86**, 4, 1984, pp. 595-601.

5. N. Bhatia and M. El-Chami, "Leadless Pacemakers: A Contemporary Review," *Journal Of Geriatric Cardiology: JGC*, **15**, 4, 2018, p. 249.

6. Y. Song, Q. Hao, K. Zhang, M. Wang, Y. Chu, and B. Kang, "The Simulation Method of the Galvanic Coupling Intrabody Communication with Different Signal Transmission Paths," *IEEE Transactions on Instrumentation and Measurement*, **60**, 4, 2010, pp. 1257-1266.

7. K. S. Cole and R. H. Cole, "Dispersion and Absorption in Dielectrics I. Alternating Current Characteristics," *The Journal of Chemical Physics*, **9**, 4, 1941, pp. 341-351.

8. C. Gabriel, et al., "The Dielectric Properties of Biological Tissues: I. Literature Survey," *Physics In Medicine & Biology*, **41**, 11, 1996, p. 2231.

9. J. Larsson, "Electromagnetics from a Quasistatic Perspective," *American Journal of Physics*, **75**, 3, 2007, pp. 230-239.

10. D. Das, et al., "Enabling Covert Body Area Network Using Electro-Quasistatic Human Body Communication," *Scientific Reports*, **9**, 1, 2019, p. 4160.

11. M. Maldari, M. Albatat, J. Bergsland, Y. Haddab, C. Jabbour, and P. Desgreys, "Wide Frequency Characterization of Intra-Body Communication for Leadless Pacemakers," *IEEE Transactions on Biomedical Engineering*, 2020.

12. A. Ng and J. Swanevelder, "Resolution in Ultrasound Imaging," *Continuing Education in Anaesthesia Critical Care & Pain*, **11**, 5, 2011, pp. 186-192.

13. J. Wang and Q. Wang, *Body Area Communications: Channel Modeling, Communication Systems, and EMC*, New York, John Wiley & Sons, 2012.

14. ICNIRP, "Guidelines for Limiting Exposure to Time-Varying Electric, Magnetic, and Electromagnetic Fields (Up to 300 GHz)," *Health Phys*., **74**, 1998, pp. 494-522.

15. L. Yan, J. Bae, S. Lee, T. Roh, K. Song, and H.-J. Yoo, "A 3.9 mw 25-Electrode Reconfigured Sensor for Wearable Cardiac Monitoring System," *IEEE Journal of Solid-State Circuits*, **46**, 1, 2010, pp. 353-364.

16. M. Haghjoo, "Pacing System Malfunction: Evaluation and Troubleshooting," in *Modern Pacemakers – Present and Future*, Rijeka: InTech, 2011, pp. 367-80.

17. P. Safavi-Naeini and M. Saeed, "Pacemaker Troubleshooting: Common Clinical Scenarios," *Texas Heart Institute Journal*, **43**, 5, 2016, pp. 415-418.

18. V. C. Campen, C. C. De Cock, J. Huijgens, and C. A. Visser, "Clinical Relevance of Loss of Atrial Sensing in Patients with Single Lead VDD Pacemakers," *Pacing and Clinical Electrophysiology*, **24**, 5, 2001, pp. 806-809.

19. U. Madhow, *Fundamentals of Digital Communication*, Cambridge University Press, 2008.

20. A. Elgani, M. Magno, F. Renzini, L. Perilli, E. F. Scarselli, A. Gnudi, R. Canegallo, G. Ricotti, and L. Benini, "Nanowatt Wake-Up Radios: Discrete-Components and Integrated Architectures," 2018 25th IEEE International Conference on Electronics, Circuits and Systems (ICECS), IEEE, 2018, pp. 793-796.

21. M. Magno and L. Benini, "An Ultra Low Power High Sensitivity Wake-Up Radio Receiver with Addressing Capability," 2014 IEEE 10th International Conference on Wireless and Mobile Computing, Networking and Communications (WiMob), IEEE, 2014, pp. 92-99.

22. S. Oh, N. E. Roberts, and D. D. Wentzloff, "A 116 nw Multiband Wake-Up Receiver with 31-Bit Correlator and Interference Rejection," Proceedings of the IEEE 2013 Custom Integrated Circuits Conference. IEEE, 2013, pp. 1-4.

23. N. E. Roberts and D. D. Wentzloff, "A 98 nw Wake-Up Radio for Wireless Body Area Networks," 2012 IEEE Radio Frequency Integrated Circuits Symposium. IEEE, 2012, pp. 373-376.

24. S. Maity, D. Yang, B. Chatterjee, and S. Sen, "A Sub-nw Wakeup Receiver for Human Body Communication," 2018 IEEE 13 Biomedical Circuits and Systems Conference (BioCAS), IEEE, 2018, pp. 1-4.

25. F. Yuan, *CMOS Circuits for Passive Wireless Microsystems*, New York, Springer Science & Business Media, 2010.

26. B. Otis and J. Rabaey, Ultra-Low Power Wireless Technologies for Sensor Networks, New York, Springer Science & Business Media, 2007.

27. H. Fuketa, S. O'uchi, and T. Matsukawa, "A 0.3-V 1-muw Superregenerative Ultrasound Wake-Up Receiver with Power Scalability," *IEEE Transactions on Circuits and Systems II: Express Briefs*, **64**, 9, 2016, pp. 1027-1031.

28. S. Alsaegh, S. A. Mohamed, and Y. Manoli, "Design of 1 mW CMOS OOK Super-Regenerative Receiver for 402-405 MHz Medical Applications," 2014 IEEE International Symposium on Circuits and Systems (ISCAS), IEEE, 2014, pp. 1400-1403.

29. J. L. Bohorquez, A. P. Chandrakasan, and J. L. Dawson, "A 350 µW CMOS MSK Transmitter and 400 µW OOK Super-Regenerative Receiver for Medical Implant Communications," *IEEE Journal of Solid-State Circuits*, **44**, 4, 2009, pp. 1248-1259.

30. N. Pekcokguler, G. Dundar, and C. Dehollain, "Analysis, Modeling and Design of a CMOS Super-Regenerative Receiver for Implanted Medical Devices Under Square and Sinusoidal Quench Signals," *Integration*, **67**, 2019, pp. 1-7.

31. V. D. Rezaei, S. J. Shellhammer, M. Elkholy, and K. Entesari, "A Fully Integrated 320 pJ/b OOK Super-Regenerative Receiver with 87 dbm Sensitivity and Self-Calibration," 2016 IEEE Radio Frequency Integrated Circuits Symposium (RFIC), IEEE, 2016, pp. 222-225.

32. J.-Y. Chen, M. P. Flynn, and J. P. Hayes, "A Fully Integrated Autocalibrated Super-Regenerative Receiver in 0:13µm CMOS," *IEEE Journal of Solid-State Circuits*, **42**, 9, 2007, pp. 1976-1985.

33. H. Cho, H. Kim, M. Kim, J. Jang, Y. Lee, K. J. Lee, J. Bae, and H.-J. Yoo, "A 79 pJ/b 80 Mb/s Full-Duplex Transceiver and a 42.5 µW 100 kb/s Super-Regenerative Transceiver for Body Channel Communication," *IEEE Journal of Solid-State Circuits*, **51**, 1, 2015, pp. 310-317.

34. A. Grebennikov, *RF and Microwave Transistor Oscillator Design*, New York, John Wiley & Sons, 2007.

35. A. Yarahmadi and A. Jannesari, "Two-Path Inverter-Based Low Noise Amplifier for 10-12 GHz Applications," *Microelectronics Journal*, **50**, 2016, pp. 76-82.

36. M. Bazes, "Two Novel Fully Complementary Self-Biased CMOS Differential Amplifiers," *IEEE Journal of Solid-State Circuits*, **26**, 2, 1991, pp. 165-168.

37. L. G´eroux, M. Limousin, and S. Cazeau, "Clinical Performances of a New Mode Switch Function Based on a Statistical Analysis of the Atrial Rhythm," *Herzschrittmachertherapie und Elektrophysiologie*, **10**, 1, 1999, pp. S15-S21.